Available online at www.sciencedirect.com
ScienceDirect
Comput. Methods Appl. Mech. Engrg. 278 (2014) 62–79
Computer methods in applied mechanics and engineering
www.elsevier.com/locate/cma

Two-scale computational homogenization of electro-elasticity at finite strains

Marc-André Keip[a,*], Paul Steinmann[b,1], Jörg Schröder[c,2]

[a] *Institute of Applied Mechanics (CE), Chair I, University of Stuttgart, Pfaffenwaldring 7, 70569 Stuttgart, Germany*
[b] *Chair of Applied Mechanics, Department of Mechanical Engineering, Friedrich-Alexander-Universität Erlangen-Nürnberg, Egerlandstr. 5, 91058 Erlangen, Germany*
[c] *Institute of Mechanics, Department of Civil Engineering, Faculty of Engineering, University of Duisburg–Essen, Universitätsstr. 15, 45141 Essen, Germany*

Received 22 January 2014; received in revised form 25 April 2014; accepted 30 April 2014
Available online 20 May 2014

Abstract

This contribution addresses a two-scale computational homogenization framework for the simulation of electro-active solids at finite strains. A generalized form of the Hill–Mandel condition is employed for the derivation of energetically consistent transition conditions between the scales. The continuum mechanical formulation is implemented into a two-scale finite element environment, in which we attach a microscopic representative volume element at each integration point of the macroscopic domain. In order to allow for an efficient solution of the macroscopic boundary value problem an algorithmically consistent tangent of the macroscopic problem is derived. The method will be applied to the analysis of dielectric polymer–ceramic composites, where we determine the effective actuation of composites with different microstructures. Furthermore, we show the applicability of the proposed method to the computation of two-scale electro-mechanically coupled boundary value problems in consideration of large deformations.

Keywords: Computational homogenization; FE^2-method; Electro-mechanical coupling; Finite deformations; Electro-active polymers; Dielectric composites

1. Introduction

The development of numerical schemes for the simulation of electro-elastic materials undergoing large strains could be helpful for the design and optimization of advanced technical applications in the area of large-strain electro-mechanical actuation like, for example, artificial muscles and robotics [1–5]. The continuum mechanical field theory for the mathematical description of the geometrically nonlinear behavior of these materials is well established [6–10] and has been employed for the modeling of electro-elasticity at finite strains [11–17]. In recent years, numerical solution methods based on different discretization techniques, mainly in the framework of finite element methods,

* Corresponding author. Tel.: +49 711 685 69261; fax: +49 711 685 66347.
E-mail addresses: keip@mechbau.uni-stuttgart.de (M.-A. Keip), paul.steinmann@ltm.uni-erlangen.de (P. Steinmann), j.schroeder@uni-due.de (J. Schröder).
[1] Tel.: +49 9131 85 28501; fax: +49 9131 85 28503.
[2] Tel.: +49 201 183 2708; fax: +49 201 183 2680.

http://dx.doi.org/10.1016/j.cma.2014.04.020
0045-7825/

have been developed [18–25]. From a practical point of view, materials with very large or "giant" electrostriction are particularly attractive. Thus, the maximization of actuation strains plays an important role in the development of electro-active elastomers. As found out experimentally, the effective electro-mechanical coupling of dielectric elastomers can be enhanced by the addition of high-electric-permittivity (high-ϵ) particles into the elastomeric matrix [26–32]. This phenomenon can be explained by the interplay between the elastomeric matrix and the inclusions, where one notes two major contributions: firstly, the overall electric permittivity is increased due to the addition of high-ϵ dispersion [26]. Secondly, the high contrast of the individual phases on the microlevel induces pronounced electric field fluctuations [33]. This interesting phenomenon is investigated theoretically by using different methods like, for example, homogenization techniques based on sequential laminates [34,35] or computational strategies based on finite element simulations [36,37], see also the works [38–40].

It should be mentioned that the addition of microstructural high-ϵ objects could lead to the important issue of microstructural instability. This can roughly be explained by the large locally induced electric fields in the elastomeric matrix which give rise to pronounced local deformations in the microstructure. In general there are two important phenomena associated with electro-mechanical instability. On the one hand instabilities occur when electrostatic forces cannot be compensated by elastic forces. On the other hand, as in any electrically charged dielectric, there is the danger of electric breakdown. For the case of homogeneous materials these issues are addressed, for example, in [41,42] for static and dynamic conditions; associated experimental observations are documented in [43]. The detailed study of the corresponding effects is however beyond the scope of the present contribution. Thus, the interested reader may be referred to, for example, the works [44–46], in which instability phenomena for composite dielectrics are analyzed in detail.

The present contribution aims at providing a *two-scale computational homogenization framework* for electro-elastic boundary value problems at finite deformations, which can be applied to the simulation, characterization and optimization of electro-elastic solids undergoing large strains. In detail, the framework is based on the FE^2-method, which solves a macroscopic boundary value problem (BVP) in consideration of the response of attached microscopic representative volume elements ($\mathcal{RVE}$). This computational method is well-established in the context of purely mechanical problems [47–58] and has been extended to the homogenization of physically coupled materials like, for example, in thermo-elasticity [59,60] and electro-mechanics [61,62]. Recently, the application to the finite-strain magneto-mechanical case was presented in [63].

The outline of the paper is as follows. In Section 2 the basic kinematical relations and balance equations of finite electro-elasticity will be summarized. Section 3 will provide the two-scale homogenization framework with a focus on the coupled BVPs on the macro- and the microscale as well as on the transition conditions between the two scales. An expression for the macroscopic tangent moduli will be given. In Section 4 the method will be applied to the simulation of polymer–ceramic composites. Section 5 will provide a short summary and a conclusion.

2. Theoretical framework

In the following we summarize the basic equations for the continuum-mechanical description of electro-elasticity at large strains. For a more detailed discussion we refer to the works [13,14] or [18].

Let the body of interest in the (undeformed) reference configuration be denoted by $\mathcal{B} \subset \mathbb{R}^3$ and parameterized in the referential coordinates $\boldsymbol{X}$; in the deformed configuration it is denoted by $\mathcal{S} \subset \mathbb{R}^3$ and is parameterized in the current coordinates $\boldsymbol{x}$. The nonlinear deformation map $\boldsymbol{\varphi}_t : \mathcal{B} \to \mathcal{S}$ at time $t \in \mathbb{R}_+$ maps points $\boldsymbol{X} \in \mathcal{B}$ onto points $\boldsymbol{x} \in \mathcal{S}$. The deformation gradient $\boldsymbol{F}$ is defined by

$$\boldsymbol{F}(\boldsymbol{X}) = \operatorname{Grad} \boldsymbol{\varphi}_t(\boldsymbol{X}) = \frac{\partial \boldsymbol{\varphi}_t(\boldsymbol{X})}{\partial \boldsymbol{X}}. \tag{1}$$

In the absence of magnetic fields and free currents the electric field in the current configuration is governed by Faraday's law of electrostatics

$$\operatorname{curl} \boldsymbol{e} = \boldsymbol{0}, \tag{2}$$

so that we can express it as the gradient of some scalar electric potential ϕ with respect to the current coordinates as

$$\boldsymbol{e} = -\operatorname{grad} \phi = -\frac{\partial \phi}{\partial \boldsymbol{x}}. \tag{3}$$

In order to formulate the mechanical balance equation we take into account that the electric field exerts a force on the material under consideration. According to e.g. [64] this force can be described by the electrostatic (or ponderomotive) body force $\boldsymbol{f}^{\text{elec}}$ given by

$$\boldsymbol{f}^{\text{elec}} = \operatorname{grad} \boldsymbol{e} \cdot \boldsymbol{p} \tag{4}$$

where $\boldsymbol{p}$ denotes the electric polarization density in the current configuration. Based on that, and in the absence of mechanical body forces, we write the balance of momentum in the current configuration as

$$\operatorname{div} \boldsymbol{\sigma}^{\text{mech}} + \boldsymbol{f}^{\text{elec}} = \boldsymbol{0}, \tag{5}$$

where $\boldsymbol{\sigma}^{\text{mech}}$ denotes the mechanical Cauchy stress tensor. In the latter equation, we can express $\boldsymbol{f}^{\text{elec}}$ in terms of the second-order Maxwell stress tensor via

$$\boldsymbol{f}^{\text{elec}} = \operatorname{div} \boldsymbol{\sigma}^{\text{elec}} \quad \text{with } \boldsymbol{\sigma}^{\text{elec}} = \boldsymbol{e} \otimes \boldsymbol{d} - \frac{1}{2}\epsilon_0 (\boldsymbol{e} \cdot \boldsymbol{e})\boldsymbol{1}, \tag{6}$$

where ϵ_0 is the permittivity of free space and $\boldsymbol{1}$ is the second-order unity tensor. Furthermore, $\boldsymbol{d}$ is the electric displacement in the current configuration given by

$$\boldsymbol{d} = \epsilon_0 \boldsymbol{e} + \boldsymbol{p}. \tag{7}$$

Thus, the balance of momentum can finally be reformulated to

$$\operatorname{div}(\boldsymbol{\sigma}^{\text{mech}} + \boldsymbol{\sigma}^{\text{elec}}) = \operatorname{div} \boldsymbol{\sigma} = \boldsymbol{0}, \tag{8}$$

where we have introduced the *total* Cauchy stress tensor $\boldsymbol{\sigma}$ which is the sum of the mechanical Cauchy stress $\boldsymbol{\sigma}^{\text{mech}}$ and the electrically induced Maxwell stress $\boldsymbol{\sigma}^{\text{elec}}$. In the absence of free charge carriers, the balance equation on the electrical side is given by Gauß's law

$$\operatorname{div} \boldsymbol{d} = 0. \tag{9}$$

In line with the work [13] we postulate the existence of a total potential Ω per unit reference volume, from which the total stresses and the electric displacements can be derived. It should be noted that this potential includes a contribution of free space, so that the Maxwell stress can also be computed for the surrounding space of the body, see e.g. [22], page 185. In order to obtain constitutive equations that satisfy *a priori* the principle of material objectivity, the functional dependence $\Omega := \psi(\boldsymbol{E}, \boldsymbol{C})$ is taken into account, where $\boldsymbol{E}$ is the electric field with respect to the reference configuration and $\boldsymbol{C}$ is the right Cauchy–Green tensor given by

$$\boldsymbol{E} = \boldsymbol{F}^T \boldsymbol{e} \quad \text{and} \quad \boldsymbol{C} = \boldsymbol{F}^T \boldsymbol{F}. \tag{10}$$

Based on the function Ω we compute the *total* second Piola–Kirchhoff stresses, the *total* first Piola–Kirchhoff stresses and the *total* Cauchy stresses by

$$\boldsymbol{S} = 2\frac{\partial \Omega}{\partial \boldsymbol{C}}, \qquad \boldsymbol{P} = \boldsymbol{F}\boldsymbol{S}, \quad \text{and} \quad \boldsymbol{\sigma} = J^{-1}\boldsymbol{F}\boldsymbol{S}\boldsymbol{F}^T, \tag{11}$$

respectively, where $J = \det \boldsymbol{F}$. The electric displacement with respect to the reference and current configuration follows consequently as

$$\boldsymbol{d} = -J^{-1}\boldsymbol{F} \cdot \frac{\partial \Omega}{\partial \boldsymbol{E}} \quad \text{and} \quad \boldsymbol{D} = J\boldsymbol{F}^{-1}\boldsymbol{d}. \tag{12}$$

3. Coupled boundary value problems on the two scales

In the framework of the FE^2-method we have to solve BVPs on two separate scales—on the macroscopic and the microscopic scale. The two associated BVPs will be discussed in the following sections based on the theoretical framework provided in Section 2. The procedures discussed below can be understood as a direct extension of the work

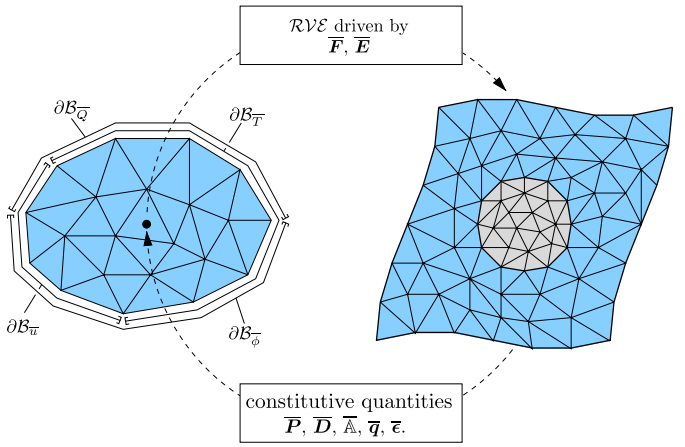

Fig. 1. Macroscopic BVP with attached $\mathcal{RVE}$ at each Gauß point. The microscopic BVP is driven by boundary conditions derived from the macroscopic deformation gradient $\overline{\boldsymbol{F}}$ and the macroscopic electric field $\overline{\boldsymbol{E}}$. An averaging process delivers the dual macroscopic quantities, i.e. the macroscopic total stresses $\overline{\boldsymbol{P}}$ and the macroscopic electric displacements $\overline{\boldsymbol{D}}$ as well as the effective elastic, electro-elastic, and dielectric moduli $\overline{\mathbb{A}}$, $\overline{\boldsymbol{q}}$, and $\overline{\boldsymbol{\epsilon}}$.

on small-strain electro-elasticity proposed in [62]. The general procedures and assumptions presented in the following trace back, amongst others, to the fundamental works on computational homogenization provided by Miehe and coworkers, see for example [48,49,53]; in this context we also refer to the summary [58]. For a visualization of the FE^2-concept see Fig. 1.

3.1. Boundary value problem on the macroscopic scale

Throughout the following sections, the quantities associated with the macroscopic scale will be labeled with an overline. Consequently, we denote the body of interest on the macroscopic scale as $\overline{\mathcal{B}} \subset \mathbb{R}^3$ and parameterize it in the coordinates $\overline{\boldsymbol{X}}$. Furthermore, the macroscopic displacement and electric potential are written as $\overline{\boldsymbol{u}}$ and $\overline{\phi}$, respectively. Based on that, we define the macroscopic deformation gradient tensor and electric field vector as

$$\overline{\boldsymbol{F}} := \overline{\operatorname{Grad}}\, \overline{\boldsymbol{x}} \quad \text{and} \quad \overline{\boldsymbol{E}} := -\overline{\operatorname{Grad}}\, \overline{\phi}. \tag{13}$$

The governing balance laws on the macroscopic scale now appear as

$$\overline{\operatorname{Div}}\, \overline{\boldsymbol{P}} = \boldsymbol{0} \quad \text{and} \quad \overline{\operatorname{Div}}\, \overline{\boldsymbol{D}} = 0 \quad \text{in } \overline{\mathcal{B}}. \tag{14}$$

We prescribe Dirichlet- and Neumann-type boundary conditions in terms of

$$\{\overline{\boldsymbol{u}}, \overline{\phi}\} = \{\overline{\boldsymbol{u}}_b, \overline{\phi}_b\} \quad \text{on } \partial\overline{\mathcal{B}}_{\{\overline{u},\overline{\phi}\}} \quad \text{and} \quad \{\overline{\boldsymbol{T}}, -\overline{Q}\} = \{[\![\overline{\boldsymbol{P}}]\!] \cdot \overline{\boldsymbol{N}}, [\![\overline{\boldsymbol{D}}]\!] \cdot \overline{\boldsymbol{N}}\} \quad \text{on } \partial\overline{\mathcal{B}}_{\{\overline{T},\overline{Q}\}} \tag{15}$$

where $\overline{\boldsymbol{T}}$ are surface tractions, $\overline{Q}$ are electric surface charges, $\overline{\boldsymbol{N}}$ is a unit normal vector pointing outwards from the body, and $[\![\bullet]\!] := \bullet_{\text{inside}} - \bullet_{\text{outside}}$ denotes the jump across the boundary of the body (note that there exists a free-space contribution of the Maxwell stress).

3.2. Micro-to-macro transitions

The above macroscopic fields $\{\overline{\boldsymbol{F}}, \overline{\boldsymbol{P}}, \overline{\boldsymbol{E}}, \overline{\boldsymbol{D}}\}$ are linked to associated microscopic counterparts $\{\boldsymbol{F}, \boldsymbol{P}, \boldsymbol{E}, \boldsymbol{D}\}$ through suitable surface integrals along the boundary $\partial\mathcal{B}$ of the microscopic representative volume element ($\mathcal{RVE}$) described on a domain $\mathcal{B}$ with volume V. By assuming continuity of the displacements and the electric potential across the $\mathcal{RVE}$ we may alternatively define the macroscopic deformation gradient and electric field through volume integrals. In this case we have

$$\overline{\boldsymbol{F}} := \langle \boldsymbol{x} \otimes \boldsymbol{N} \rangle_{\partial\mathcal{B}} = \langle \boldsymbol{F} \rangle_{\mathcal{B}} \quad \text{and} \quad \overline{\boldsymbol{E}} := \langle -\phi\, \boldsymbol{N} \rangle_{\partial\mathcal{B}} = \langle \boldsymbol{E} \rangle_{\mathcal{B}} \tag{16}$$

where $\langle\bullet\rangle_{\partial\mathcal{B}} := \frac{1}{V}\int_{\partial\mathcal{B}} \bullet \, dA$ denotes the average of the surface integral along $\partial\mathcal{B}$ and $\langle\bullet\rangle_{\mathcal{B}} := \frac{1}{V}\int_{\mathcal{B}} \bullet \, dV$ denotes the average of the volume integral over the $\mathcal{RVE}$ with respect to the reference state. Furthermore, $\boldsymbol{N}$ is a unit normal vector pointing outwards from the $\mathcal{RVE}$. In addition to that we define the macroscopic Piola stresses and electric displacements as

$$\overline{\boldsymbol{P}} := \langle \boldsymbol{T} \otimes \boldsymbol{X}\rangle_{\partial\mathcal{B}} = \langle \boldsymbol{P}\rangle_{\mathcal{B}} \quad \text{and} \quad \overline{\boldsymbol{D}} := \langle -Q\, \boldsymbol{X}\rangle_{\partial\mathcal{B}} = \langle \boldsymbol{D}\rangle_{\mathcal{B}}. \tag{17}$$

Please note that the equality of the surface and volume integrals in (17) is only valid when mechanical body forces and free electric charge carriers are neglected on the microscale. For a detailed derivation of the relations given in (16) and (17) in the small-strain setting see [65].

3.3. Boundary value problem on the microscopic scale

The quantities on the microscopic scale will have no special labeling. We denote the microscopic body as $\mathcal{B} \subset \mathbb{R}^3$ and parameterize it in the microscopic coordinates $\boldsymbol{x}$. In analogy to (13) the microscopic deformation gradient and electric field are given by

$$\boldsymbol{F} := \mathrm{Grad}\boldsymbol{x} \quad \text{and} \quad \boldsymbol{E} := -\mathrm{Grad}\phi. \tag{18}$$

The balance equations are written down as

$$\mathrm{Div}\,\boldsymbol{P} = \boldsymbol{0} \quad \text{and} \quad \mathrm{Div}\,\boldsymbol{D} = 0 \quad \text{in } \mathcal{B}, \tag{19}$$

where we have neglected body forces as well as charge carriers on the microscale. Appropriate boundary conditions on $\partial\mathcal{B}$ can be derived from a generalized form of the classical Hill–Mandel macro-homogeneity condition [66]

$$\dot{\overline{\Omega}} = \langle \dot{\Omega}\rangle_{\mathcal{B}} \quad \Leftrightarrow \quad \overline{\boldsymbol{P}} : \dot{\overline{\boldsymbol{F}}} - \overline{\boldsymbol{D}} \cdot \dot{\overline{\boldsymbol{E}}} = \langle \boldsymbol{P} : \dot{\boldsymbol{F}}\rangle_{\mathcal{B}} - \langle \boldsymbol{D} \cdot \dot{\boldsymbol{E}}\rangle_{\mathcal{B}}, \tag{20}$$

refer to [61,62] for the electro-mechanically coupled case in the small-strain setting. This condition is fulfilled if

$$\mathcal{P} := \underbrace{\langle \boldsymbol{P} : \dot{\boldsymbol{F}}\rangle_{\mathcal{B}} - \overline{\boldsymbol{P}} : \dot{\overline{\boldsymbol{F}}}}_{\mathcal{P}_1} + \underbrace{\overline{\boldsymbol{D}} \cdot \dot{\overline{\boldsymbol{E}}} - \langle \boldsymbol{D} \cdot \dot{\boldsymbol{E}}\rangle_{\mathcal{B}}}_{\mathcal{P}_2} = 0, \tag{21}$$

see [61] for a detailed discussion on how to fulfill this condition by setting $\mathcal{P}_1 = 0$ and $\mathcal{P}_2 = 0$ individually. The simplest assumption of the microscopic fields that automatically satisfy the above condition is given by postulating the constraints $\boldsymbol{P} := \overline{\boldsymbol{P}}$ or $\dot{\boldsymbol{F}} := \dot{\overline{\boldsymbol{F}}}$ and $\boldsymbol{D} := \overline{\boldsymbol{D}}$ or $\dot{\boldsymbol{E}} := \dot{\overline{\boldsymbol{E}}}$, which are associated to the Sachs–Reuss and Voigt–Taylor bounds, respectively. More general boundary conditions can be derived from an equivalent expression[3] of (21) given by

$$\mathcal{P} = \underbrace{\langle [\boldsymbol{T} - \overline{\boldsymbol{P}} \cdot \boldsymbol{N}] \cdot [\dot{\boldsymbol{u}} - \dot{\overline{\boldsymbol{F}}} \cdot \boldsymbol{X}]\rangle_{\partial\mathcal{B}}}_{\widehat{\mathcal{P}}_1} + \underbrace{\langle [Q + \overline{\boldsymbol{D}} \cdot \boldsymbol{N}]\, [\dot{\phi} + \dot{\overline{\boldsymbol{E}}} \cdot \boldsymbol{X}]\rangle_{\partial\mathcal{B}}}_{\widehat{\mathcal{P}}_2} = 0. \tag{22}$$

From the conditions $\widehat{\mathcal{P}}_1 = 0$ and $\widehat{\mathcal{P}}_2 = 0$ we derive the Dirichlet and Neumann boundary conditions in terms of the mechanical and electrical quantities as

$$\{\dot{\boldsymbol{u}}, \dot{\phi}\} = \{\dot{\overline{\boldsymbol{F}}} \cdot \boldsymbol{X}, -\dot{\overline{\boldsymbol{E}}} \cdot \boldsymbol{X}\} \quad \text{and} \quad \{\boldsymbol{T}, Q\} = \{\overline{\boldsymbol{P}} \cdot \boldsymbol{N}, -\overline{\boldsymbol{D}} \cdot \boldsymbol{N}\} \quad \text{on } \partial\mathcal{B}, \tag{23}$$

respectively. Periodic boundary conditions satisfying the two individual conditions are given by

$$\{\boldsymbol{T}, Q\}(\boldsymbol{X}^+) = -\{\boldsymbol{T}, Q\}(\boldsymbol{X}^-) \quad \text{and} \quad \{\widetilde{\boldsymbol{w}}, \widetilde{\phi}\}(\boldsymbol{X}^+) = \{\widetilde{\boldsymbol{w}}, \widetilde{\phi}\}(\boldsymbol{X}^-) \quad \text{on } \boldsymbol{X}^\pm \in \partial\mathcal{B}^\pm, \tag{24}$$

where $\widetilde{\boldsymbol{w}}$ and $\widetilde{\phi}$ are the microscopic fluctuations of the displacement and the electric potential and $\boldsymbol{X}^\pm \in \partial\mathcal{B}^\pm$ denote points on opposite faces of the $\mathcal{RVE}$.

[3] For a detailed derivation of this expression we refer to the Appendix B.

3.4. Algorithmically consistent linearization of macroscopic field equations

In order to obtain quadratic convergence within the Newton scheme on the macroscopic scale we must linearize the macroscopic weak forms consistently. This goes along with the consistent linearization of the macroscopic total Piola stresses and the macroscopic electric displacements

$$\Delta\overline{\boldsymbol{P}} = \frac{\partial\overline{\boldsymbol{P}}}{\partial\overline{\boldsymbol{F}}} : \Delta\overline{\boldsymbol{F}} + \frac{\partial\overline{\boldsymbol{P}}}{\partial\overline{\boldsymbol{E}}} \cdot \Delta\overline{\boldsymbol{E}} \quad \text{and} \quad \Delta\overline{\boldsymbol{D}} = \frac{\partial\overline{\boldsymbol{D}}}{\partial\overline{\boldsymbol{F}}} : \Delta\overline{\boldsymbol{F}} + \frac{\partial\overline{\boldsymbol{D}}}{\partial\overline{\boldsymbol{E}}} \cdot \Delta\overline{\boldsymbol{E}}. \tag{25}$$

Taking into account the definitions (17) we note that we have to compute the partial derivatives of volume averages with respect to the macroscopic deformation gradient and electric field, i.e.

$$\overline{\mathbb{A}} := \frac{\partial\langle\boldsymbol{P}\rangle_{\mathcal{B}}}{\partial\overline{\boldsymbol{F}}}, \qquad \overline{\boldsymbol{q}} := \frac{\partial\langle\boldsymbol{D}\rangle_{\mathcal{B}}}{\partial\overline{\boldsymbol{F}}} = \left[-\frac{\partial\langle\boldsymbol{P}\rangle_{\mathcal{B}}}{\partial\overline{\boldsymbol{E}}}\right]^{T} \quad \text{and} \quad \overline{\boldsymbol{\epsilon}} := \frac{\partial\langle\boldsymbol{D}\rangle_{\mathcal{B}}}{\partial\overline{\boldsymbol{E}}}. \tag{26}$$

Here we introduced the macroscopic mechanical moduli $\overline{\mathbb{A}}$, dielectric moduli $\overline{\boldsymbol{\epsilon}}$, and electro-elastic moduli $\overline{\boldsymbol{q}}$ with $[\overline{\boldsymbol{q}}^{T}]_{ijk} := \overline{q}_{kij}$.

In order to derive suitable measures for the effective coefficients we assume that the microscopic deformation gradient and electric field (18) can be decomposed into constant parts $\{\overline{\boldsymbol{F}}, \overline{\boldsymbol{E}}\}$ and fluctuating parts $\{\widetilde{\boldsymbol{F}}, \widetilde{\boldsymbol{E}}\}$ so that

$$\{\boldsymbol{F}, \boldsymbol{E}\} := \{\overline{\boldsymbol{F}}, \overline{\boldsymbol{E}}\} + \{\widetilde{\boldsymbol{F}}, \widetilde{\boldsymbol{E}}\} \quad \text{with} \int_{\mathcal{B}} \{\widetilde{\boldsymbol{F}}, \widetilde{\boldsymbol{E}}\}\, dV = \boldsymbol{0}. \tag{27}$$

Here it should be noted that $(27)_2$ is automatically satisfied through the definitions of the boundary conditions formulated in (23) and (24). By using the above superposition principle together with the chain rule we can rewrite (25) as

$$\begin{bmatrix} \Delta\overline{\boldsymbol{P}} \\ -\Delta\overline{\boldsymbol{D}} \end{bmatrix} = \frac{1}{V}\left(\int_{\mathcal{B}} \begin{bmatrix} \mathbb{A} & -\boldsymbol{q}^{T} \\ -\boldsymbol{q} & -\boldsymbol{\epsilon} \end{bmatrix} + \begin{bmatrix} \mathbb{A} : \dfrac{\partial\widetilde{\boldsymbol{F}}}{\partial\overline{\boldsymbol{F}}} & -\boldsymbol{q}^{T} \cdot \dfrac{\partial\widetilde{\boldsymbol{E}}}{\partial\overline{\boldsymbol{E}}} \\ -\boldsymbol{q} : \dfrac{\partial\widetilde{\boldsymbol{F}}}{\partial\overline{\boldsymbol{F}}} & -\boldsymbol{\epsilon} \cdot \dfrac{\partial\widetilde{\boldsymbol{E}}}{\partial\overline{\boldsymbol{E}}} \end{bmatrix} dV\right) \begin{bmatrix} \Delta\overline{\boldsymbol{F}} \\ \Delta\overline{\boldsymbol{E}} \end{bmatrix}, \tag{28}$$

where we introduced the algorithmically consistent microscopic elastic, electro-elastic, and dielectric tangent moduli as the partial derivatives

$$\mathbb{A} := \frac{\partial\boldsymbol{P}}{\partial\boldsymbol{F}}, \qquad \boldsymbol{q} := \frac{\partial\boldsymbol{D}}{\partial\boldsymbol{F}} = -\left[\frac{\partial\boldsymbol{P}}{\partial\boldsymbol{E}}\right]^{T}, \quad \text{and} \quad \boldsymbol{\epsilon} := \frac{\partial\boldsymbol{D}}{\partial\boldsymbol{E}}. \tag{29}$$

In Eq. (28) we have to compute partial derivatives of the microscopic fluctuation fields with respect to their macroscopic counterparts. This can be done by using the FE discretization of the microscopic $\mathcal{RVE}$ which gives us the algorithmically consistent macroscopic moduli in matrix notation as

$$\begin{bmatrix} \overline{\underline{\mathsf{A}}} & -\overline{\underline{\mathsf{q}}}^{\mathsf{T}} \\ -\overline{\underline{\mathsf{q}}} & -\overline{\underline{\epsilon}} \end{bmatrix} = \frac{1}{V}\int_{\mathcal{B}} \begin{bmatrix} \underline{\mathsf{A}} & -\underline{\mathsf{q}}^{\mathsf{T}} \\ -\underline{\mathsf{q}} & -\underline{\epsilon} \end{bmatrix} dV - \frac{1}{V}\begin{bmatrix} \underline{\mathsf{L}}_{\mathsf{uu}} & \underline{\mathsf{L}}_{\mathsf{u}\phi} \\ \underline{\mathsf{L}}_{\phi\mathsf{u}} & \underline{\mathsf{L}}_{\phi\phi} \end{bmatrix}^{\mathsf{T}} \begin{bmatrix} \underline{\mathsf{K}}_{\mathsf{uu}} & \underline{\mathsf{K}}_{\mathsf{u}\phi} \\ \underline{\mathsf{K}}_{\phi\mathsf{u}} & \underline{\mathsf{K}}_{\phi\phi} \end{bmatrix}^{-1} \begin{bmatrix} \underline{\mathsf{L}}_{\mathsf{uu}} & \underline{\mathsf{L}}_{\mathsf{u}\phi} \\ \underline{\mathsf{L}}_{\phi\mathsf{u}} & \underline{\mathsf{L}}_{\phi\phi} \end{bmatrix}.$$

Here the first term on the right hand side constitutes a simple volume average of the algorithmic microscopic moduli over the $\mathcal{RVE}$. The second term arises as an augmentation of the macroscopic moduli that results from the incorporation of microscopic fluctuations on the $\mathcal{RVE}$. For a straightforward derivation and the definition of the used matrices see Appendix A.

4. Numerical examples

In the following sections we will apply the proposed method to the two-scale simulation of dielectric polymer–ceramic composites. First, the influence of the dielectric properties of ceramic inclusions on the overall actuation of an electroactive composite will be analyzed. Based on that, we will investigate the overall performance in consideration of different volume fractions and different shapes of the inclusions. Finally, the method will be employed for the

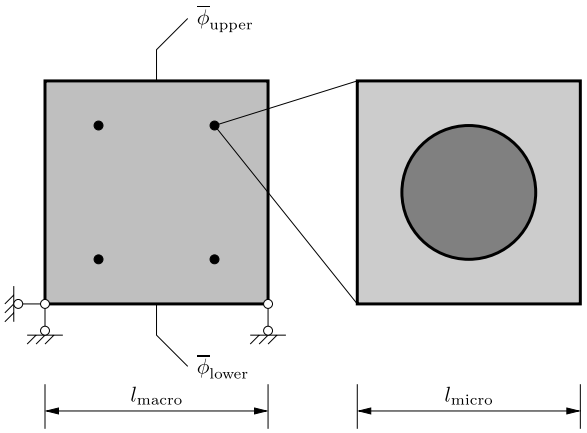

Fig. 2. Macroscopic boundary value problem with $\mathcal{RVE}$ attached at each integration point (for simplicity, only one finite element on the macroscopic scale is depicted). The $\mathcal{RVE}$ is composed of a polymer matrix and a ceramic inclusion. On the macroscopic scale we consider a statically determined body with prescribed electric potential boundary conditions on its upper and lower surface. On the microscopic scale we consider periodic boundary conditions. Please note that $l_{\text{micro}} \ll l_{\text{macro}}$.

two-scale simulation of a macroscopic electric bimorph with attached microscopic $\mathcal{RVE}$s. In all simulations we consider periodic boundary conditions on the microscale and describe both, elastomer and ceramic inclusions, by the Neo-Hookean-type potential

$$\widehat{\Omega}(\boldsymbol{C},\boldsymbol{E}) = \frac{1}{2}\mu(\text{tr}[\boldsymbol{C}]-3) + \frac{\lambda}{4}(J^2-1) - \left(\frac{\lambda}{2}+\mu\right)\ln J - \frac{1}{2}\epsilon_0\left(1+\frac{\chi}{J}\right) J\,[\boldsymbol{C}^{-1}:(\boldsymbol{E}\otimes\boldsymbol{E})], \tag{30}$$

where λ and μ are the Lamé constants and χ is the electric susceptibility, from which the latter is defined to be zero in free space and greater than zero in dielectric materials.

4.1. Computational homogenization of polymer–ceramic composites

Experimental investigations show that the overall actuation performance of a dielectric polymer can be enhanced by the usage of composite materials, see the short discussion in the introduction. As indicated there, one of the reasons for that lies in the fact that the actuation of a non-polar (non-piezoelectric or -ferroelectric) dielectric is mainly governed by the electrostatic body forces (or Maxwell stresses). From the constitutive viewpoint, the Maxwell stress itself is a function of the dielectric properties of the material. Since elastomers generally have comparably small susceptibility in the order of magnitude $\chi \approx 10^1$, the addition of metal or ceramic inclusions (as for instance barium titanate which has a susceptibility with order of magnitude of $\chi \approx 10^3$)[4] can significantly enhance the overall susceptibility. Next to that, the high contrast of the matrix and the inclusions leads to electric field fluctuations on the microscale, which induce electric field gradients and thus give rise to the appearance of electrostatic body forces. The following numerical examples will investigate the overall coupling of ceramic-reinforced dielectric elastomers.

In detail, we investigate the effective response of some idealized composite $\mathcal{RVE}$s that have to be imagined as periodically embedded in an overall macroscopic body. For the analysis of the composite we use the above presented homogenization framework, which means that we attach an $\mathcal{RVE}$ at each integration point of the macroscopic domain, see Fig. 2.

As depicted in the figure the loading is given by an electric potential difference applied to the macroscopic body. By using the periodic boundary conditions derived in Section 3 the primary gradient fields in each integration point of the macroscopic body are transferred to the attached $\mathcal{RVE}$s. Then, after the solution of the associated microscopic boundary value problem, the effective response is given back to the macroscale. In each integration point, the effective response includes the effective stresses, the effective electric displacements as well as the effective material moduli of

[4] A metal is a conductor and thus has $\chi \to \infty$. This often leads to a pronounced enhancement of the actuation. We will, however, concentrate on the analysis of polymer composites made from ceramics.

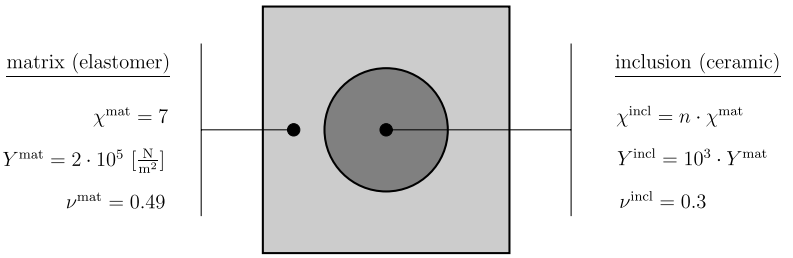

Fig. 3. Dielectric polymer–ceramic composite with different susceptibilities of the inclusion. In this example, the volume fraction of the inclusion is 20%. Both, matrix and inclusion are described with the Neo-Hookean potential given in (30). The size of the $\mathcal{RVE}$ is $1 \cdot 10^{-3} \times 1 \cdot 10^{-3}$ [mm^2].

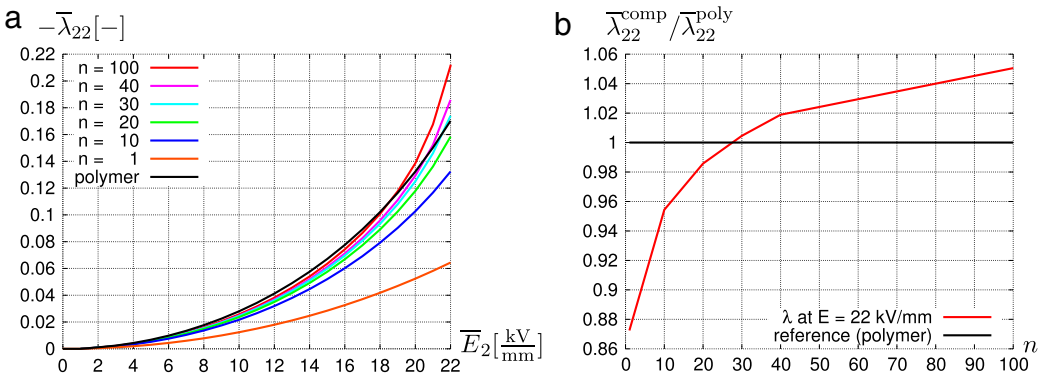

Fig. 4. Actuation of the composite under applied macroscopic electric field $\overline{E}_2$: (a) development of actuation in consideration of different dielectric properties of the inclusion $\chi^{\mathrm{incl}} = n \cdot \chi^{\mathrm{mat}}$ (polymer deformation is given as reference), (b) relative deformation under applied electric field of $\overline{E}_2 = 22\ [\frac{\mathrm{kV}}{\mathrm{mm}}]$ for the different composites (the relative deformation is computed as the ratio between composite deformation $\overline{\lambda}_{22}^{\mathrm{comp}}$ and polymer deformation $\overline{\lambda}_{22}^{\mathrm{poly}}$ parallel to the applied electric field).

the composite microstructure. For the numerical solution of the boundary value problems on the microscale we use homogeneous finite element discretizations with six-noded triangular finite elements. The number of elements in each $\mathcal{RVE}$ is about 1000, which was found to be a sufficient discretization for the computation of quantitatively meaningful results.

4.1.1. Analysis of the influence of the dielectric properties of the inclusion

In order to quantify the influence of the dielectric properties of the inclusion we analyze the overall behavior of an elastomer with circular ceramic inclusions[5] that have different susceptibility, see Fig. 3.

The susceptibility of the inclusions will be chosen as $n = 1, 10, 20, 30, 40, 100$ times the susceptibility of the elastomer, i.e. $\chi^{\mathrm{incl}} = n \cdot \chi^{\mathrm{mat}}$ with $\chi^{\mathrm{mat}} = 7$. We choose the Young modulus of the inclusion to be 10^3 times the Young modulus of the matrix with $Y^{\mathrm{mat}} = 2 \cdot 10^5\ [\frac{\mathrm{N}}{\mathrm{m}^2}]$, i.e. $Y^{\mathrm{incl}} = 10^3 \cdot Y^{\mathrm{mat}} = 2 \cdot 10^8\ [\frac{\mathrm{N}}{\mathrm{m}^2}]$. In order to account for the nearly incompressible character of the matrix we set Poisson's ratio[6] to $\nu^{\mathrm{mat}} = 0.49$. Poisson's ratio of the inclusion is set to $\nu^{\mathrm{incl}} = 0.3$. For the present analysis we consider a volume fraction of the inclusion of 20%.

As electric boundary conditions we prescribe a positive electric potential $\overline{\phi}_{\mathrm{lower}}$ on the lower surface and a negative potential $\overline{\phi}_{\mathrm{upper}}$ on the upper surface, so that the specimen is loaded with a homogeneous macroscopic electric field $\overline{E}_2$ that points in positive vertical direction. Fig. 4 shows the development of macroscopic actuation strain $\overline{\lambda}_{22}$ with respect to the applied macroscopic electric field. Furthermore, the achievable maximum strains under the macroscopic field $\overline{E}_2 = 22\ [\frac{\mathrm{kV}}{\mathrm{mm}}]$ are compared to the strain obtained with the polymer alone.

[5] In the present two-dimensional study such a composite constitutes a dielectric elastomer with periodically arranged cylindrical fibers.

[6] It should be mentioned that the electro-elastic response of the elastomer is sensitive of the choice of Poisson's ratio. For simulations in the quasi-incompressible limit ($\nu \to 0.5$) the usage of mixed finite element formulations will thus be favorable, see, for example, [25,67].

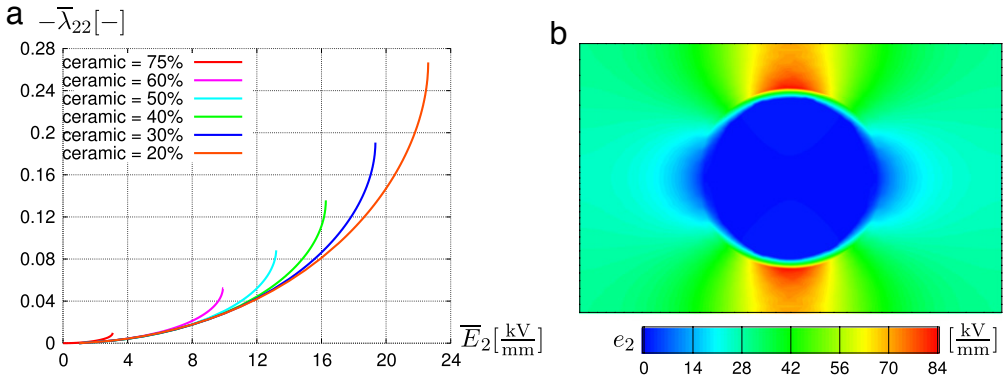

Fig. 5. Actuation under applied electric field of the composite: (a) development of actuation in consideration of different volume fractions of the inclusion. With increasing volume fraction of the inclusion instabilities of the composite are induced already under smaller applied fields. As can be seen clearly, the initiation of instability goes along with a vertical tangent of the individual actuation curves. The source of the overall instabilities however originates from effects occurring on the lower scale, see b): due to the higher stiffness of the inclusion and the high electric field gradients above and below the inclusion, deformations are mainly induced locally in the matrix material. The regions above and below the inclusions experience a pronounced compressive strain of approximately 50% that makes the matrix unstable. With increasing volume fraction of the inclusion this local strain is generated already under lower fields. The contour shows the vertical microscopic current electric field e_2 of the microstructure with 20% volume fraction of the inclusion under macroscopic loading of $\overline{E}_2 = 22\,[\frac{\text{kV}}{\text{mm}}]$.

Clearly, the actuation of the material can be enhanced by the addition of ceramic particles. As can be seen, an increase in actuation for the present setup can already be achieved by the addition of particles with a susceptibility that is approximately 30 times the susceptibility of the matrix.

4.1.2. Analysis of the influence of the volume fraction of the inclusion

In the above simulation we investigated the overall behavior of a composite with a constant volume fraction of the inclusion of 20%. It can be expected that the volume fraction of the inclusion will have an impact on the macroscopic response. Thus, the following analysis will focus on composite materials that are composed of different fractions of inclusion and matrix material. The shape of the inclusion will again be assumed to be circular, now having a fraction of 20, 30, 40, 50, 60, and 75%, respectively.[7] In all computations, the susceptibility of the inclusion is set to $\chi^{\text{incl}} = 100 \cdot \chi^{\text{mat}}$. The results are shown in Fig. 5.

As expected, the magnitude of actuation strains under identical fields is higher for the composites with higher volume fraction. However, we observe that the initiation of instabilities is also a function of the volume fraction in the sense that instabilities arise under smaller fields when the inclusion fraction is increased. Clear indicators for the initiation of instabilities are the vertical tangents of the individual actuation curves. It is however enlightening to note that the source of the observed overall instabilities originates from effects occurring on the lower scale. This can be explained as follows. Since the inclusion material is stiff compared to the matrix, deformations mainly occur in the matrix material. Furthermore, since the susceptibility of the inclusion is 100 times higher than that of the matrix, the electric potential inside the inclusion has a small gradient resulting in a small electric field inside the inclusion. On the other hand, high electric fields and high electric field gradients arise above and below the inclusion, see Fig. 5(b). In order to give a clear impression on the amount of the generated electric field gradients a three-dimensional surface plot of the vertical electric field in the microstructure is shown in Fig. 6.

The described effects yield pronounced electrically induced deformations *locally* above and below the inclusion (strains of the order of magnitude of approximately 50% are observed). This finally leads to *local* instabilities which are initiated earlier when the amount of inclusion material is increased. We conclude that in composites the appearance of instabilities may be associated to microscopic phenomena. This is then clearly dependent on the morphology of the microstructure as well as on the properties of the individual phases. For a detailed analysis of instability phenomena in dielectric composites see, for example, [44–46].

[7] In the present context of a circular inclusion inside a rectangular matrix the upper bound of the volume fraction for non-overlapping inclusions is given by 78,54 %.

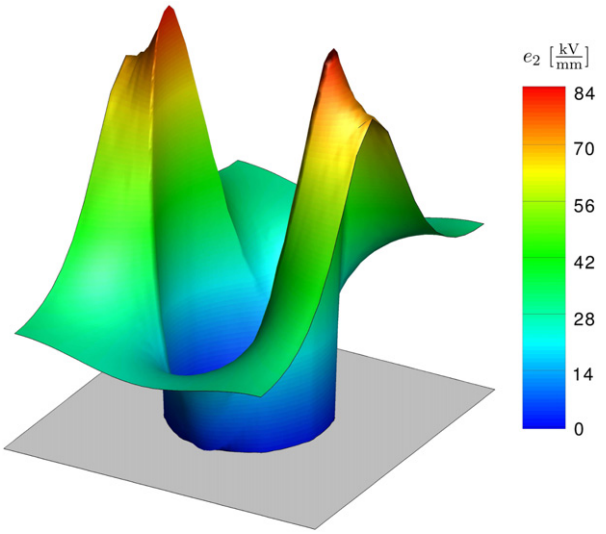

Fig. 6. Three-dimensional plot of the current electric field within the microstructure with 20% volume fraction of the inclusion. It becomes obvious that high gradients of the electric field occur above and below the inclusion. The contour shows the microscopic electric field component parallel to the applied macroscopic field $\overline{E}_2 = 22$ [kV/mm].

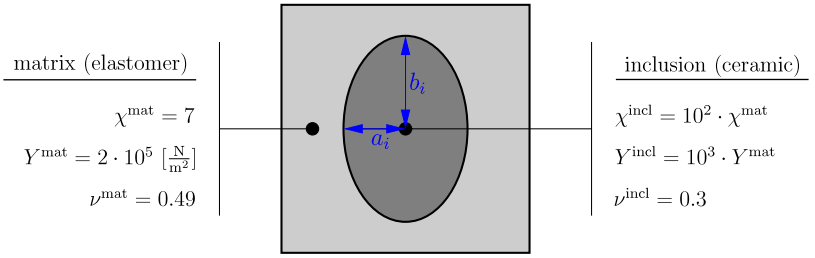

Fig. 7. Dielectric polymer–ceramic composite with ellipsoidal inclusions. We consider ellipsoidal inclusions with volume fractions of 20, 30, and 40%. The individual dimensions are given by $\{a, b\}_{20} = \{0.1706, 0.3732\}$, $\{a, b\}_{30} = \{0.2424, 0.3939\}$, and $\{a, b\}_{40} = \{0.3708, 0.4136\}$ [10^{-3} mm]. The outer dimensions of the $\mathcal{RVE}$ are $1 \cdot 10^{-3} \times 1 \cdot 10^{-3}$ [mm^2].

4.1.3. Analysis of the influence of the shape of the inclusion

Next, we investigate the actuation response in consideration of different inclusion geometries. Here, we will focus on inclusions with ellipsoidal shape and consider the composites with volume fractions of 20, 30, and 40%.[8] The dimensions of the individual ellipsoids are given by $\{a, b\}_{20} = \{0.1706, 0.3732\}$, $\{a, b\}_{30} = \{0.2424, 0.3939\}$, and $\{a, b\}_{40} = \{0.3708, 0.4136\}$, all in [$10^{-3}$ mm]. As in the previous computations, the dimensions of the $\mathcal{RVE}$ are given by $1 \cdot 10^{-3} \times 1 \cdot 10^{-3}$ [mm^2]. In Fig. 7 a composite structure with ellipsoidal inclusion is depicted.

We now analyze the coupling behavior of these composites under two different loading scenarios. In the first case we apply a macroscopic electric field that points parallel to the major axes of the ellipsoids, i.e. a field that is aligned with the major axes. In the second case we rotate the electric field by 90° so that it is oriented perpendicular to the major axes of the ellipsoids. The results of the computations are shown in Fig. 8. Here we compared the individual coupling responses also to the coupling of the composites with circular inclusions and identical volume fractions.

In Fig. 8(a) we observe that the shape of the inclusions has a significant influence on the overall response of the composite. On the one hand, applying electric fields perpendicular to the major axes (i.e. in horizontal direction in Fig. 8) gives a soft reaction with comparably large obtainable deformations. On the other hand, applying the electric field parallel to the major axes of the inclusions gives a pronounced electro-active response already under small fields.

[8] The inclusions of the composites with higher volume fractions can poorly be transferred into an ellipsoidal shape with representative character since the boundary of the inclusion is close to the boundary of the $\mathcal{RVE}$.

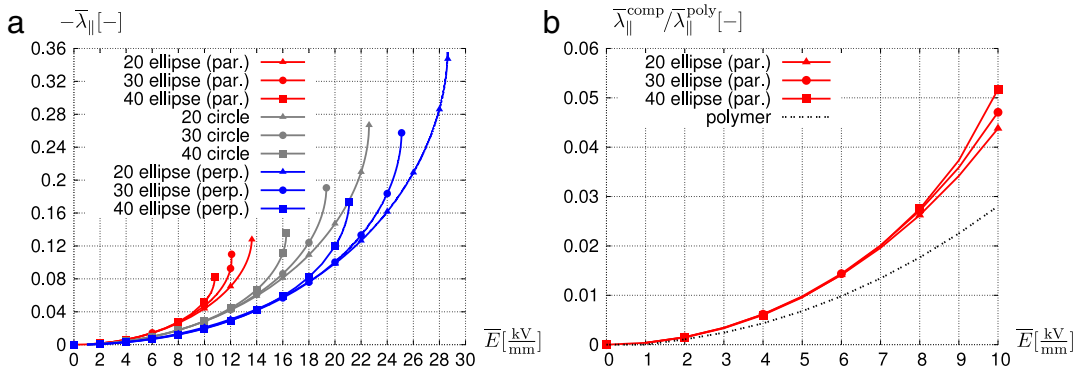

Fig. 8. Actuation under applied electric field of the composite: (a) development of actuation in consideration of different shapes of the inclusion for the volume fractions 20, 30, and 40% ($\chi^{\text{incl}} = 100 \cdot \chi^{\text{mat}}$; "par." and "perp." mean that the applied electric field is oriented parallel and perpendicular to the major axis of the ellipse, respectively); (b) response of the three composites with parallel loading in the small-electric-field regime. Note that under an applied field of for instance $\overline{E}_2 = 7\,[\frac{\text{kV}}{\text{mm}}]$ the actuation is increased by approximately 50% irrespective of the volume fraction of the inclusion.

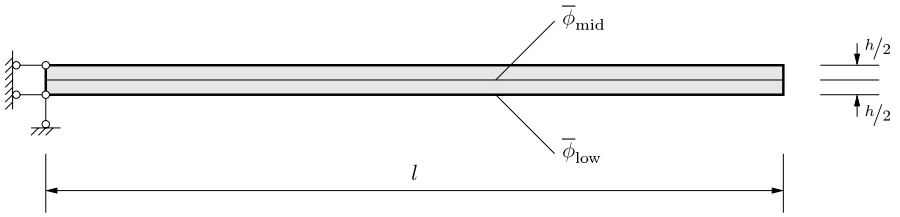

Fig. 9. The macroscopic boundary value problem is given by an electric bimorph with dimensions of $l = 100\,[\text{mm}]$ and $h = 1\,[\text{mm}]$. As electric boundary conditions we apply zero electric potential at the lower boundary of the specimen ($\overline{\phi}_{\text{low}} = 0\,[\text{kV}]$) and a linearly increasing electric potential through its center ($\overline{\phi}_{\text{mid}} \geq 0\,[\text{kV}]$). The electric potential at the upper boundary is left free. The mechanical boundary conditions are prescribed in such a way that the left end of the specimen is fixed in horizontal direction and the lower left corner is fixed in both horizontal and vertical direction. At each macroscopic Gauß point we attach an $\mathcal{RVE}$ composed of a polymer matrix and a circular ceramic inclusion with a volume fraction of 20% and $\chi^{\text{incl}} = 100 \cdot \chi^{\text{mat}}$.

In these cases, the electro-mechanical coupling is the highest. When the composites are loaded in this way they show, however, unstable behavior already at smaller fields compared to the others.

A remarkable outcome of the present computations is revealed by the comparison between the composites with vertical ellipsoidal inclusions in the small-electric-field range, see Fig. 8(b). There we clearly observe that the response of the three composites is nearly identical irrespective of e.g. a doubling in volume fraction from 20 to 40%. For instance under an applied macroscopic field of $\overline{E}_2 = 7\,[\frac{\text{kV}}{\text{mm}}]$, the actuation is increased by approximately 50% for all considered volume fractions of the inclusion. We conclude that, next to the volume fraction, the shape of the inclusions is a predominant input variable that can be optimized in the development of dielectric composites; in this context see, for example, [35].

4.2. *Two-scale simulation of an electric bimorph*

In order to show the general functionality of the proposed two-scale formulation we now consider the simulation of an electro-active bimorph with composite microstructure. The macroscopic boundary value problem is depicted in Fig. 9.

The bimorph consists of two layers that are connected through an electrode which is located between the two layers. At the bottom of the bimorph a second electrode in attached. The driving mechanism of the bimorph is based on the potential difference between the lower and the middle electrode and its interaction with the upper (passive) layer: due to the potential difference between the two electrodes an electric field in thickness direction is induced only in the lower half of the specimen. This gives rise to a local contraction of the material which yields expansion in the

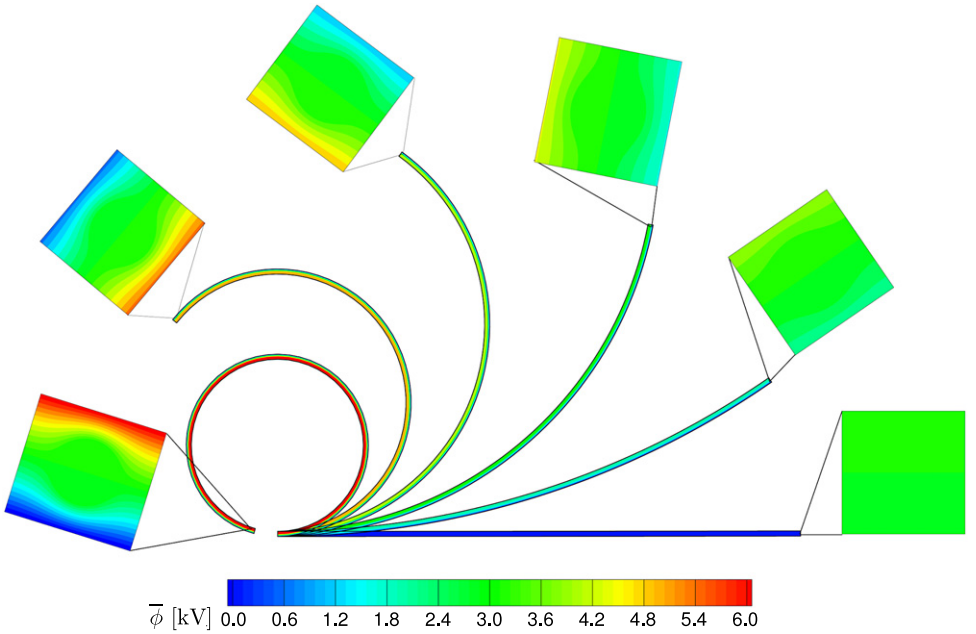

Fig. 10. Stepwise deformation of the bimorph under applied macroscopic electric potentials $\overline{\phi}_{\text{mid}} = 0,\ 2,\ 3,\ 4,\ 5,\ 6\,[\text{kV}]$ together with deformed exemplary $\mathcal{RVE}$s at the tip of the cantilever. Note, that the legend refers to the macroscopic electric potential. On the microscale we compute the electric potential from (49) so that in each $\mathcal{RVE}$ a *local* distribution of electric potential is obtained. Adding the corresponding (constant) macroscopic part would not change the situation so that it is simply omitted.

direction perpendicular to the field. Since the upper layer is not electrically activated it acts as a passive component and restrains lateral deformation. Thus, bending of the cantilever is initiated.

In order to study the deformation of the bimorph under applied electric fields, we discretize it with 100 quadratic triangular finite elements with six nodes and three Gauß points. At each Gauß point we attach a microscopic $\mathcal{RVE}$ that is discretized with 1,168 six-noded triangular elements. The $\mathcal{RVE}$s are composed of a polymeric matrix and a circular ceramic inclusion with a volume fraction of 20%. We employ the same material parameters as in the foregoing studies and choose a susceptibility of the inclusion of $\chi^{\text{incl}} = 100 \cdot \chi^{\text{mat}}$. As electric boundary conditions we apply zero electric potential at the lower boundary of the specimen ($\overline{\phi}_{\text{low}} = 0\,[\text{kV}]$) and a non-zero electric potential on its center electrode ($\overline{\phi}_{\text{mid}} \geq 0\,[\text{kV}]$). The electric potential at the upper boundary is left free. The mechanical boundary conditions are prescribed in such a way that the nodes at the left end of the specimen are fixed in horizontal direction and the lower left node is fixed completely. The deformation of the bimorph under linearly increasing loading as well as deformations of an exemplary $\mathcal{RVE}$ at the tip of the cantilever are shown in Fig. 10.

We see clearly the resulting pronounced deformations on the macroscale as well as the heterogeneous reactions on the microscale. In the final stage of loading the tip of the specimen and the attached $\mathcal{RVE}$ have performed nearly a full rotation with respect to the out-of-plane normal. It is remarkable that, although the local deformations (strains) in the $\mathcal{RVE}$ are rather small, the overall rotations of the cantilever are very large. This is due to the slender geometry of the specimen. In this slender configuration, already small strains are able to produce large rotations.

5. Summary and conclusion

We have presented a two-scale finite-element (FE^2) framework for the simulation of electro-elastic materials at finite strains. The method was derived based on classical micro–macro transition conditions for electro-mechanical fields. The microscopic boundary value problem was defined on periodic representative volume elements. In order to account for the effect of electrostatic volume forces we employed the concept of Maxwell stress on the microscale. The overall macroscopic response was computed by suitable averaging processes over the microscale.

The presented method was then applied to the simulation of electro-elastic polymer-matrix composites with ceramic inclusions. The influence of the inclusion's dielectric properties on the overall coupling was analyzed in

detail. In addition to that, different volume fractions of circular as well as ellipsoidal inclusions were studied. The simulations confirmed that the actuation performance of a soft polymer can significantly be enhanced by adding ceramic dispersions. Here, next to electric properties and volume fraction, the shape of the inclusion has shown a major influence on the overall actuation. This reveals the inclusion shape as an important design variable for the development of dielectric composites with enhanced properties.

Finally, we applied the framework to the two-scale simulation of an electro-mechanical boundary value problem given by an electric bimorph actuator. The simulations showed that the method can be used for the detailed study of electro-elastic coupling phenomena of soft materials at finite deformations on two separate scales.

Acknowledgments

The financial support of the German Research Foundation (DFG) in the framework of the Research Group FOR 1509 "Ferroic Functional Materials - Multiscale Modeling and Experimental Characterization" (projects SCHR 570/12-1 and STE 544/47-1) as well as in the framework of the Cluster of Excellence in "Simulation Technology" (EXC 310/2) at the University of Stuttgart, are gratefully acknowledged.

Appendix A. Computation of macroscopic tangent

In order to derive the effective macroscopic tangent we consider the discrete forms of the coupled BVP on the microscale. We first summarize the basic ingredients for the solution of the microscopic BVP like, for example, the weak formulation and its FE implementation (the strategy follows classical "standard" procedures of FE methods). After that we arrive at the macroscopic tangent by conducting a sensitivity analysis of the microscopic BVP at an equilibrium state. For the small-strain analog to the following procedure see [62].

Weak formulation. The weak form of the balance of linear momentum in the referential setting appears as

$$G_u = -\int_{\mathcal{B}} \mathrm{Div}\boldsymbol{P}\cdot\delta\widetilde{\boldsymbol{w}}\,dV = \underbrace{\int_{\mathcal{B}}\delta\widetilde{\boldsymbol{F}}:\boldsymbol{P}\,dV}_{G_u^{\mathrm{int}}} \underbrace{-\int_{\partial\mathcal{B}}\delta\widetilde{\boldsymbol{w}}\cdot(\boldsymbol{P}\cdot\boldsymbol{N})\,dA}_{G_u^{\mathrm{ext}}} \tag{31}$$

and the corresponding weak form of Gauß's law of electrostatics is given by

$$G_\phi = -\int_{\mathcal{B}} \mathrm{Div}\boldsymbol{D}\,\delta\widetilde{\phi}\,dV = \underbrace{-\int_{\mathcal{B}}\delta\widetilde{\boldsymbol{E}}\cdot\boldsymbol{D}\,dV}_{G_\phi^{\mathrm{int}}} \underbrace{-\int_{\partial\mathcal{B}}\delta\widetilde{\phi}(\boldsymbol{D}\cdot\boldsymbol{N})\,dA}_{G_\phi^{\mathrm{ext}}}. \tag{32}$$

Here we introduced $\widetilde{\boldsymbol{F}} = \mathrm{Grad}\,\delta\widetilde{\boldsymbol{w}}$ and $\delta\widetilde{\boldsymbol{E}} := -\mathrm{Grad}\,\delta\widetilde{\phi}$. The linearization of the above weak forms yields under the assumption of conservative loadings the linear increment of the virtual mechanical work

$$\Delta G_u = \Delta G_u^{\mathrm{int}} = \int_{\mathcal{B}}\delta\widetilde{\boldsymbol{F}}:\mathbb{A}:\Delta\widetilde{\boldsymbol{F}}\,dV - \int_{\mathcal{B}}\delta\widetilde{\boldsymbol{F}}:\boldsymbol{q}^T\cdot\Delta\widetilde{\boldsymbol{E}}\,dV, \tag{33}$$

with $[\boldsymbol{q}^T]_{\mathrm{ijk}} := q_{\mathrm{kij}}$. Furthermore we calculate the incremental virtual electrical work as

$$\Delta G_\phi = \Delta G_\phi^{\mathrm{int}} = -\int_{\mathcal{B}}\delta\widetilde{\boldsymbol{E}}\cdot\boldsymbol{q}:\Delta\widetilde{\boldsymbol{F}}\,dV - \int_{\mathcal{B}}\delta\widetilde{\boldsymbol{E}}\cdot\boldsymbol{\epsilon}\cdot\Delta\widetilde{\boldsymbol{E}}\,dV. \tag{34}$$

Finite element approximation. In order to ease the readability of the following derivations we shortly note some details on the used (standard) FE implementation on the microscale. Here we make use of vector-matrix notation, where all appearing vectors and matrices are labeled with an underline (for example $\boldsymbol{u} \rightarrow \underline{\mathsf{u}}$). The vector notations of the deformation gradient tensor and of the total first Piola–Kirchhoff stress tensor are assumed as follows

$$\begin{aligned}\underline{\mathsf{F}} &= [\mathsf{F}_{11},\mathsf{F}_{22},\mathsf{F}_{33},\mathsf{F}_{12},\mathsf{F}_{23},\mathsf{F}_{13},\mathsf{F}_{21},\mathsf{F}_{32},\mathsf{F}_{31}]^{\mathsf{T}},\\ \underline{\mathsf{P}} &= [\mathsf{P}_{11},\mathsf{P}_{22},\mathsf{P}_{33},\mathsf{P}_{12},\mathsf{P}_{23},\mathsf{P}_{13},\mathsf{P}_{21},\mathsf{P}_{32},\mathsf{P}_{31}]^{\mathsf{T}},\end{aligned} \tag{35}$$

respectively. In the framework of the discretization of the weak forms on the microscale we consider the fluctuations of the displacements and of the electric potential. The approximations of the fluctuation fields as well as of their virtual

and incremental counterparts appear in a classical fashion as

$$\{\widetilde{\underline{w}},\, \delta\widetilde{\underline{w}},\, \Delta\widetilde{\underline{w}}\} = \underline{N}^{e}_{u}\, \{\widetilde{\underline{d}}^{e}_{u},\, \delta\widetilde{\underline{d}}^{e}_{u},\, \Delta\widetilde{\underline{d}}^{e}_{u}\} \quad \text{and} \quad \{\widetilde{\phi},\, \delta\widetilde{\phi},\, \Delta\widetilde{\phi}\} = \underline{N}^{e}_{\phi}\, \{\widetilde{\underline{d}}^{e}_{\phi},\, \delta\widetilde{\underline{d}}^{e}_{\phi},\, \Delta\widetilde{\underline{d}}^{e}_{\phi}\} \tag{36}$$

where $\underline{N}^{e}_{\{u,\phi\}}$ are the interpolation functions associated to the nodes of each finite element and $\widetilde{\underline{d}}^{e}_{u,\phi}$ denote the element degrees of freedom. The approximations of the fluctuations of the deformation gradient and of the electric field are given correspondingly by

$$\{\widetilde{\underline{F}},\, \delta\widetilde{\underline{F}},\, \Delta\widetilde{\underline{F}}\} = \underline{B}^{e}_{u}\, \{\widetilde{\underline{d}}^{e}_{u},\, \delta\widetilde{\underline{d}}^{e}_{u},\, \Delta\widetilde{\underline{d}}^{e}_{u}\} \quad \text{and} \quad \{\widetilde{\underline{E}},\, \delta\widetilde{\underline{E}},\, \Delta\widetilde{\underline{E}}\} = \underline{B}^{e}_{\phi}\, \{\widetilde{\underline{d}}^{e}_{\phi},\, \delta\widetilde{\underline{d}}^{e}_{\phi},\, \Delta\widetilde{\underline{d}}^{e}_{\phi}\}, \tag{37}$$

where $\underline{B}^{e}_{\{u,\phi\}}$ contain derivatives of the interpolation functions. We insert the above expressions into the linear increments of the weak forms (33) and (34) and obtain the discrete representation of the mechanical and the electric part as

$$\Delta G^{h}_{u} = \sum_{e=1}^{n_{elem}} \delta\widetilde{\underline{d}}^{e,T}_{u} \Big[\underbrace{\int_{\mathcal{B}^e} \underline{B}^{e,T}_{u}\, \underline{A}\, \underline{B}^{e}_{u}\, dV}_{\underline{k}^{e}_{uu}}\, \Delta\widetilde{\underline{d}}^{e}_{u} - \underbrace{\int_{\mathcal{B}^e} \underline{B}^{e,T}_{u}\, \underline{q}^{T}\, \underline{B}^{e}_{\phi}\, dV}_{\underline{k}^{e}_{u\phi}}\, \Delta\widetilde{\underline{d}}^{e}_{\phi} \Big],$$

$$\Delta G^{h}_{\phi} = \sum_{e=1}^{n_{elem}} \delta\widetilde{\underline{d}}^{e,T}_{\phi} \Big[\underbrace{-\int_{\mathcal{B}^e} \underline{B}^{e,T}_{\phi}\, \underline{q}\, \underline{B}^{e}_{u}\, dV}_{\underline{k}^{e}_{\phi u}}\, \Delta\widetilde{\underline{d}}^{e}_{u} \underbrace{-\int_{\mathcal{B}^e} \underline{B}^{e,T}_{\phi}\, \underline{\epsilon}\, \underline{B}^{e}_{\phi}\, dV}_{\underline{k}^{e}_{\phi\phi}}\, \Delta\widetilde{\underline{d}}^{e}_{\phi} \Big].$$

with the associated matrix notation of the mechanical, electro-elastic, and dielectric moduli $\underline{A}$, $\underline{q}$, and $\underline{\epsilon}$, respectively. Taking into account a number of n_{elem} finite elements of the microscopic BVP, the assembling procedure yields the compact notation

$$\sum_{e=1}^{n_{elem}} \begin{bmatrix} \delta\widetilde{\underline{d}}^{e}_{u} \\ \delta\widetilde{\underline{d}}^{e}_{\phi} \end{bmatrix}^{T} \left(\underbrace{\begin{bmatrix} \underline{k}^{e}_{uu} & \underline{k}^{e}_{u\phi} \\ \underline{k}^{e}_{\phi u} & \underline{k}^{e}_{\phi\phi} \end{bmatrix}}_{\underline{k}^{e}} \underbrace{\begin{bmatrix} \Delta\widetilde{\underline{d}}^{e}_{u} \\ \Delta\widetilde{\underline{d}}^{e}_{\phi} \end{bmatrix}}_{\Delta\widetilde{\underline{d}}^{e}_{u,\phi}} + \underbrace{\begin{bmatrix} \underline{r}^{e}_{u} \\ \underline{r}^{e}_{\phi} \end{bmatrix}}_{\underline{r}^{e}} \right) = 0,$$

with the element residual vectors $\underline{r}^{e}_{u,\phi}$ resulting from the discrete counterparts of (31) and (32). Above, we identify the complete element stiffness matrix $\underline{k}^{e}$ the incremental element solution vector $\Delta\widetilde{\underline{d}}^{e}_{u,\phi}$, and the element residual vector $\underline{r}^{e}$. The solution of the global problem gives the global solution vector

$$\Delta\widetilde{\underline{D}}_{u,\phi} = -\underline{K}^{-1}\underline{R} \tag{38}$$

with the global stiffness matrix and the global residual vector

$$\underline{K} = \mathop{\mathsf{A}}_{e=1}^{n_{elem}} \underline{k}^{e} \quad \text{and} \quad \underline{R} = \mathop{\mathsf{A}}_{e=1}^{n_{elem}} \underline{r}^{e}, \tag{39}$$

where the A denotes suitable assembly operators. Note that the global solution vector should not be confused with the vector notation of the fluctuations of the electric displacements.

Computation of algorithmically consistent macroscopic tangent. In order to derive the algorithmically consistent macroscopic tangent from (28) we linearize the microscopic weak forms at an equilibrium state

$$\int_{\mathcal{B}} \delta\widetilde{\boldsymbol{F}} : \mathbb{A} : (\Delta\overline{\boldsymbol{F}} + \Delta\widetilde{\boldsymbol{F}})\, dV - \int_{\mathcal{B}} \delta\widetilde{\boldsymbol{F}} : \boldsymbol{q}^{T} \cdot (\Delta\overline{\boldsymbol{E}} + \Delta\widetilde{\boldsymbol{E}})\, dV = 0,$$

$$-\int_{\mathcal{B}} \delta\widetilde{\boldsymbol{E}} \cdot \boldsymbol{q} : (\Delta\overline{\boldsymbol{F}} + \Delta\widetilde{\boldsymbol{F}})\, dV - \int_{\mathcal{B}} \delta\widetilde{\boldsymbol{E}} \cdot \boldsymbol{\epsilon} \cdot (\Delta\overline{\boldsymbol{E}} + \Delta\widetilde{\boldsymbol{E}})\, dV = 0.$$

and insert the FE approximations (37). Then we achieve the relation for the mechanical part

$$\sum_{e=1}^{n_{elem}} \delta\widetilde{\underline{d}}_u^{e,T} \Big[\underbrace{\int_{\mathcal{B}^e} \underline{B}_u^{e,T}\, \underline{A}\, dV}_{\underline{l}_{uu}^e}\, \Delta\underline{\overline{F}} + \underbrace{\int_{\mathcal{B}^e} \underline{B}_u^{e,T}\, \underline{A}\, \underline{B}_u^e\, dV}_{\underline{k}_{uu}^e}\, \Delta\widetilde{\underline{d}}_u^e - \underbrace{\int_{\mathcal{B}^e} \underline{B}_u^{e,T}\, \underline{q}^T\, dV}_{\underline{l}_{u\phi}^e}\, \Delta\underline{\overline{E}} - \underbrace{\int_{\mathcal{B}^e} \underline{B}_u^{e,T}\, \underline{q}^T\, \underline{B}_\phi^e\, dV}_{\underline{k}_{u\phi}^e}\, \Delta\widetilde{\underline{d}}_\phi^e \Big] = 0 \tag{40}$$

where we have defined suitable FE l-matrices. Analogously we obtain

$$\sum_{e=1}^{n_{elem}} (\delta\widetilde{\underline{d}}_\phi^e)^T \Big[\underbrace{-\int_{\mathcal{B}^e} \underline{B}_\phi^{e,T}\, \underline{q}\, dV}_{underline\underline{l}_{\phi u}^e}\, \Delta\underline{\overline{F}} \underbrace{-\int_{\mathcal{B}^e} \underline{B}_\phi^{e,T}\, \underline{q}\, \underline{B}_u^e\, dV}_{\underline{k}_{\phi u}^e}\, \Delta\widetilde{\underline{d}}_u^e - \underbrace{\int_{\mathcal{B}^e} \underline{B}_\phi^{e,T}\, \underline{\epsilon}\, dV}_{\underline{l}_{\phi\phi}^e}\, \Delta\underline{\overline{E}} - \underbrace{\int_{\mathcal{B}^e} \underline{B}_\phi^{e,T}\, \underline{\epsilon}\, \underline{B}^e\, dV}_{\underline{k}_{\phi\phi}^e}\, \Delta\widetilde{\underline{d}}_\phi^e \Big] = 0. \tag{41}$$

We arrive at the compact notations of (40) and (41)

$$\begin{aligned} &\sum_{e=1}^{n_{elem}} \delta\widetilde{\underline{d}}_u^{e,T} [\, \underline{l}_{uu}^e\, \Delta\underline{\overline{F}} + \underline{k}_{uu}^e\, \Delta\widetilde{\underline{d}}_u^e + \underline{l}_{u\phi}^e\, \Delta\underline{\overline{E}} + \underline{k}_{u\phi}^e\, \Delta\widetilde{\underline{d}}_\phi^e\,] = 0, \\ &\sum_{e=1}^{n_{elem}} \delta\widetilde{\underline{d}}_\phi^{e,T} [\, \underline{l}_{\phi u}^e\, \Delta\underline{\overline{F}} + \underline{k}_{\phi u}^e\, \Delta\widetilde{\underline{d}}_u^e + \underline{l}_{\phi\phi}^e\, \Delta\underline{\overline{E}} + \underline{k}_{\phi\phi}^e\, \Delta\widetilde{\underline{d}}_\phi^e\,] = 0. \end{aligned} \tag{42}$$

Using the FE assembling procedure we write this statement in the global setting

$$\begin{bmatrix} \delta\widetilde{\underline{D}}_u \\ \delta\widetilde{\underline{D}}_\phi \end{bmatrix}^T \left(\begin{bmatrix} \underline{K}_{uu} & \underline{K}_{u\phi} \\ \underline{K}_{\phi u} & \underline{K}_{\phi\phi} \end{bmatrix} \begin{bmatrix} \Delta\widetilde{\underline{D}}_u \\ \Delta\widetilde{\underline{D}}_\phi \end{bmatrix} + \begin{bmatrix} \underline{L}_{uu}\, \Delta\underline{\overline{F}} + \underline{L}_{u\phi}\, \Delta\underline{\overline{E}} \\ \underline{L}_{\phi u}\, \Delta\underline{\overline{F}} + \underline{L}_{\phi\phi}\, \Delta\underline{\overline{E}} \end{bmatrix} \right) = 0 \tag{43}$$

where we have assembled the global stiffness and L-matrices

$$\{\underline{K}, \underline{L}\}_{ij} = \mathop{\mathsf{A}}_{e=1}^{n_{elem}} \{\underline{k}^e, \underline{l}^e\}_{ij} \quad \text{with } i, j := \{u, \phi\}. \tag{44}$$

From (43) we formally compute the incremental nodal fluctuations as

$$\begin{bmatrix} \Delta\widetilde{\underline{D}}_u \\ \Delta\widetilde{\underline{D}}_\phi \end{bmatrix} = - \begin{bmatrix} \underline{K}_{uu} & \underline{K}_{u\phi} \\ \underline{K}_{\phi u} & \underline{K}_{\phi\phi} \end{bmatrix}^{-1} \begin{bmatrix} \underline{L}_{uu}\, \Delta\underline{\overline{F}} + \underline{L}_{u\phi}\, \Delta\underline{\overline{E}} \\ \underline{L}_{\phi u}\, \Delta\underline{\overline{F}} + \underline{L}_{\phi\phi}\, \Delta\underline{\overline{E}} \end{bmatrix}. \tag{45}$$

The effective macroscopic moduli can now be derived by using the finite element approximations of the deformation gradient and the electric field (37). We insert them, together with the L-Matrices (44) into the Eq. (28) so that we achieve the matrix form of the effective macroscopic moduli

$$\begin{bmatrix} \overline{\underline{A}} & -\overline{\underline{q}}^T \\ -\overline{\underline{q}} & -\overline{\underline{\epsilon}} \end{bmatrix} = \frac{1}{V} \int_{\mathcal{B}} \begin{bmatrix} \underline{A} & -\underline{q}^T \\ -\underline{q} & -\underline{\epsilon} \end{bmatrix} dV + \frac{1}{V} \begin{bmatrix} \underline{L}_{uu} & \underline{L}_{u\phi} \\ \underline{L}_{\phi u} & \underline{L}_{\phi\phi} \end{bmatrix}^T \begin{bmatrix} \dfrac{\partial}{\partial\underline{\overline{F}}} \Delta\widetilde{\underline{D}}_u \\ \dfrac{\partial}{\partial\underline{\overline{E}}} \Delta\widetilde{\underline{D}}_\phi \end{bmatrix}. \tag{46}$$

The partial derivatives of the incremental fluctuations with respect to the macroscopic gradient fields can be computed on the basis of the solution of the global BVP (45) as follows

$$\begin{bmatrix} \frac{\partial}{\partial \overline{\underline{F}}} \Delta \widetilde{\underline{D}}_u \\ \frac{\partial}{\partial \overline{\underline{E}}} \Delta \widetilde{\underline{D}}_\phi \end{bmatrix} = - \begin{bmatrix} \underline{K}_{uu} & \underline{K}_{u\phi} \\ \underline{K}_{\phi u} & \underline{K}_{\phi\phi} \end{bmatrix}^{-1} \begin{bmatrix} \underline{L}_{uu} & \underline{L}_{u\phi} \\ \underline{L}_{\phi u} & \underline{L}_{\phi\phi} \end{bmatrix}. \tag{47}$$

Finally, inserting this result into (46) gives us the algorithmically consistent macroscopic moduli as

$$\begin{bmatrix} \overline{\underline{A}} & -\overline{\underline{q}}^{\mathsf{T}} \\ -\overline{\underline{q}} & -\overline{\underline{\epsilon}} \end{bmatrix} = \frac{1}{V} \int_{\mathcal{B}} \begin{bmatrix} \underline{A} & -\underline{q}^{\mathsf{T}} \\ -\underline{q} & -\underline{\epsilon} \end{bmatrix} dV - \frac{1}{V} \begin{bmatrix} \underline{L}_{uu} & \underline{L}_{u\phi} \\ \underline{L}_{\phi u} & \underline{L}_{\phi\phi} \end{bmatrix}^{\mathsf{T}} \begin{bmatrix} \underline{K}_{uu} & \underline{K}_{u\phi} \\ \underline{K}_{\phi u} & \underline{K}_{\phi\phi} \end{bmatrix}^{-1} \begin{bmatrix} \underline{L}_{uu} & \underline{L}_{u\phi} \\ \underline{L}_{\phi u} & \underline{L}_{\phi\phi} \end{bmatrix}.$$

Appendix B. Reformulation of Hill–Mandel condition

In order to derive suitable boundary conditions on the microscale we reformulated the Hill–Mandel condition (21) into the expression (22). This reformulation can be obtained by some consecutive steps, which are briefly summarized in the following. Here we will exemplarily concentrate on the electrical contribution only. The following derivations are a direct extension of the elementary ideas provided in [48,49,53,51] to electrostatic quantities.

As a first step, we take into account that the electric field is defined as the negative gradient of the electric potential, so that the second volume integral in (21) can be mapped onto the surface of the $\mathcal{RVE}$ via

$$\langle \boldsymbol{D} \cdot \dot{\boldsymbol{E}} \rangle_{\mathcal{B}} = -\langle \boldsymbol{D} \cdot \operatorname{Grad} \dot{\phi} \rangle_{\mathcal{B}} = -\langle \operatorname{Div} (\boldsymbol{D}\, \dot{\phi}) - \underbrace{\operatorname{Div} \boldsymbol{D}}_{=0}\, \dot{\phi} \rangle_{\mathcal{B}} = -\langle (\boldsymbol{D} \cdot \boldsymbol{N})\, \dot{\phi} \rangle_{\partial\mathcal{B}}, \tag{48}$$

where we consecutively used the product rule, Gauß's law $(19)_2$, and the divergence theorem. Now, by using the definition of the microscopic electric potential and the superposition principle of the electric displacement

$$\dot{\phi} = -\dot{\overline{\boldsymbol{E}}} \cdot \boldsymbol{X} + \dot{\widetilde{\phi}} \quad \text{and} \quad \boldsymbol{D} := \overline{\boldsymbol{D}} + \widetilde{\boldsymbol{D}}, \tag{49}$$

respectively, the last term in the latter equation can further be transformed into

$$-\langle (\boldsymbol{D} \cdot \boldsymbol{N})\, \dot{\phi} \rangle_{\partial\mathcal{B}} = -\overline{\boldsymbol{D}} \cdot \underbrace{\langle \boldsymbol{N}\, \dot{\widetilde{\phi}} \rangle_{\partial\mathcal{B}}}_{=0} - \langle (\widetilde{\boldsymbol{D}} \cdot \boldsymbol{N})\, \dot{\widetilde{\phi}} \rangle_{\partial\mathcal{B}} + \dot{\overline{\boldsymbol{E}}} \cdot \langle (\boldsymbol{D} \cdot \boldsymbol{N}) \boldsymbol{X} \rangle_{\partial\mathcal{B}}. \tag{50}$$

Here we extracted the macroscopic (constant) quantities $\overline{\boldsymbol{D}}$ and $\dot{\overline{\boldsymbol{E}}}$ from the volume integrals and noticed that the remaining surface integral of the first term on the right-hand side vanishes by definition $(27)_2$. Furthermore, the last term on the right-hand side can be recast in

$$\dot{\overline{\boldsymbol{E}}} \cdot \langle (\boldsymbol{D} \cdot \boldsymbol{N})\, \boldsymbol{X} \rangle_{\partial\mathcal{B}} = -\dot{\overline{\boldsymbol{E}}} \cdot \langle Q\, \boldsymbol{X} \rangle_{\partial\mathcal{B}} = \dot{\overline{\boldsymbol{E}}} \cdot \overline{\boldsymbol{D}} \tag{51}$$

where we used $(17)_2$. Combining the latter equation with (48) and (50) gives the relation

$$\underbrace{\overline{\boldsymbol{D}} \cdot \dot{\overline{\boldsymbol{E}}} - \langle \boldsymbol{D} \cdot \dot{\boldsymbol{E}} \rangle_{\mathcal{B}}}_{=: \mathcal{P}_2} = -\langle (\widetilde{\boldsymbol{D}} \cdot \boldsymbol{N})\, \dot{\widetilde{\phi}} \rangle_{\partial\mathcal{B}} \tag{52}$$

so that, by taking into account that $\mathcal{P}_2 = 0$ in (21), we arrive at

$$-\langle (\widetilde{\boldsymbol{D}} \cdot \boldsymbol{N})\, \dot{\widetilde{\phi}} \rangle_{\partial\mathcal{B}} = 0. \tag{53}$$

By again using the relations given in (49) we arrive finally at

$$-\langle (\widetilde{\boldsymbol{D}} \cdot \boldsymbol{N})\, \dot{\widetilde{\phi}} \rangle_{\partial\mathcal{B}} = \underbrace{\langle [Q + \overline{\boldsymbol{D}} \cdot \boldsymbol{N}]\, [\dot{\phi} + \dot{\overline{\boldsymbol{E}}} \cdot \boldsymbol{X}] \rangle_{\partial\mathcal{B}}}_{\widehat{\mathcal{P}}_2} = 0 \tag{54}$$

which is identical to the expression that has been given in (22). The above procedure can analogously be applied to the mechanical part of the Hill–Mandel condition.

References

[1] R. Pelrine, R. Kornbluh, Q. Pei, J. Joseph, High-speed electrically actuated elastomers with strain greater than 100%, Science 287 (5454) (2000) 836–839.
[2] Y. Bar-Cohen (Ed.), Electroactive Polymer (EAP) Actuators as Artificial Muscles: Reality, Potential, and Challenges, SPIE Press, Bellingham, 2001.
[3] K. J. Kim, S. Tadokoro, Electroactive Polymers for Robotics Applications: Artificial Muscles and Sensors, Springer, 2007.
[4] G. Kovacs, P. Lochmatter, M. Wissler, An arm wrestling robot driven by dielectric elastomer actuators, Smart Mater. Struct. 16 (2) (2007) S306.
[5] F. Carpi, D. De Rossi, R. Kornbluh, R. E. Pelrine, P. Sommer-Larsen (Eds.), Dielectric Elastomers as Electromechanical Transducers: Fundamentals, Materials, Devices, Models and Applications of An Emerging Electroactive Polymer Technology, Elsevier, 2011.
[6] R. A. Toupin, The elastic dielectric, J. Ration. Mech. Anal. 5 (6) (1956) 849–915.
[7] A. C. Eringen, On the foundations of electroelastostatics, Int. J. Eng. Sci. 1 (1) (1963) 127–153.
[8] G. Maugin, Continuum Mechanics of Electromagnetic Solids, vol. 33, North-Holland, Amsterdam, 1988.
[9] A.C. Eringen, G.A. Maugin, Electrodynamics of Continua, Springer, New York, 1990.
[10] A. Kovetz, Electromagnetic Theory, Oxford University Press, Oxford, 2000.
[11] K. Bhattacharya, J. Li, Y. Xiao, Electromechanical models for optimal design and effective behavior of electroactive polymers, in: Y. Bar-Cohen (Ed.), Electroactive Polymer (EAP) Actuators as Artificial Muscles: Reality, Potential, and Challenges, SPIE Press, Bellingham, 2001, pp. 309–330.
[12] R.M. McMeeking, C.M. Landis, Electrostatic forces and stored energy for deformable dielectric materials, J. Appl. Mech. 72 (4) (2005) 581–590.
[13] A. Dorfmann, R.W. Ogden, Nonlinear electroelasticity, Acta Mater. 174 (3–4) (2005) 167–183.
[14] A. Dorfmann, R.W. Ogden, Nonlinear electroelastic deformations, J. Elasticity 82 (2) (2006) 99–127.
[15] N.C. Goulbourne, E.M. Mockensturm, M.I. Frecker, Electro-elastomers: large deformation analysis of silicone membranes, Int. J. Solids Struct. 44 (9) (2007) 2609–2626.
[16] Z. Suo, X. Zhao, W.H. Greene, A nonlinear field theory of deformable dielectrics, J. Mech. Phys. Solids 56 (2) (2008) 467–486.
[17] R. Bustamante, A. Dorfmann, R.W. Ogden, On electric body forces and maxwell stresses in nonlinearly electroelastic solids, Int. J. Eng. Sci. 47 (11) (2009) 1131–1141.
[18] D.K. Vu, P. Steinmann, G. Possart, Numerical modelling of non-linear electroelasticity, Int. J. Numer. Methods Eng. 70 (6) (2007) 685–704.
[19] D.K. Vu, P. Steinmann, Nonlinear electro- and magneto-elastostatics: material and spatial settings, Int. J. Solids Struct. 44 (24) (2007) 7891–7905.
[20] S. Skatulla, A. Arockiarajan, C. Sansour, A nonlinear generalized continuum approach for electro-elasticity including scale effects, J. Mech. Phys. Solids 57 (1) (2009) 137–160.
[21] D.K. Vu, P. Steinmann, A 2-d coupled bem–fem simulation of electro-elastostatics at large strain, Comput. Methods Appl. Mech. Engrg. 199 (17) (2010) 1124–1133.
[22] P. Steinmann, Computational nonlinear electro-elasticity—getting started, in: R.W. Ogden, D.J. Steigmann (Eds.), Mechanics and Electrodynamics of Magneto-and Electro-elastic Materials, in: CISM International Centre for Mechanical Sciences, vol. 527, Springer, 2011, pp. 181–230.
[23] S. Skatulla, C. Sansour, A. Arockiarajan, A multiplicative approach for nonlinear electro-elasticity, Comput. Methods Appl. Mech. Engrg. 245–246 (2012) 243–255.
[24] A. Ask, A. Menzel, M. Ristinmaa, Electrostriction in electro-viscoelastic polymers, Mech. Mater. 50 (2012) 9–21.
[25] S. Klinkel, S. Zwecker, R. Müller, A solid shell finite element formulation for dielectric elastomers, J. Appl. Mech. 80 (2013) 021026–1–11.
[26] Q.M. Zhang, H. Li, M. Poh, F. Xia, Z.-Y. Cheng, H. Xu, C. Huang, An all-organic composite actuator material with a high dielectric constant, Nature 419 (6904) (2002) 284–287.
[27] C. Huang, Q.M. Zhang, J. Su, High-dielectric-constant all-polymer percolative composites, Appl. Phys. Lett. 82 (20) (2003) 3502–3504.
[28] C. Huang, Q.M. Zhang, G. DeBotton, K. Bhattacharya, All-organic dielectric-percolative three-component composite materials with high electromechanical response, Appl. Phys. Lett. 84 (22) (2004) 4391–4393.
[29] C. Huang, Q.M. Zhang, J.Y. Li, M. Rabeony, Colossal dielectric and electromechanical responses in self-assembled polymeric nanocomposites, Appl. Phys. Lett. 87 (18) (2005) 182901–182901–3.
[30] J.Y. Li, C. Huang, Q.M. Zhang, Enhanced electromechanical properties in all-polymer percolative composites, Appl. Phys. Lett. 84 (16) (2004) 3124–3126.
[31] F. Carpi, D.D. Rossi, Improvement of electromechanical actuating performances of a silicone dielectric elastomer by dispersion of titanium dioxide powder, IEEE Trans. Dielectr. Electr. Insul. 12 (4) (2005) 835–843.
[32] S. Zhang, C. Huang, R.J. Klein, F. Xia, Q.M. Zhang, Z.-Y. Cheng, High performance electroactive polymers and nano-composites for artificial muscles, J. Intell. Mater. Syst. Struct. 18 (2) (2007) 133–145.
[33] L. Tian, L. Tevet-Deree, G. DeBotton, K. Bhattacharya, Dielectric elastomer composites, J. Mech. Phys. Solids 60 (1) (2012) 181–198.
[34] G. DeBotton, L. Tevet-Deree, E.A. Socolsky, Electroactive heterogeneous polymers: analysis and applications to laminated composites, Mech. Adv. Mat. Str. 14 (1) (2007) 13–22.
[35] S. Rudykh, A. Lewinstein, G. Uner, G. deBotton, Analysis of microstructural induced enhancement of electromechanical coupling in soft dielectrics, Appl. Phys. Lett. 102 (15) (2013) 151905.

[36] R. Müller, B.-X. Xu, D. Gross, M. Lyschik, D. Schrade, S. Klinkel, Deformable dielectrics—optimization of heterogeneities, Int. J. Eng. Sci. 48 (7) (2010) 647–657.
[37] M. Klassen, B.-X. Xu, S. Klinkel, R. Müller, Material modeling and microstructural optimization of dielectric elastomer actuators, Techn. Mech. 32 (1) (2012) 38–52.
[38] P. Ponte Castañeda, M.H. Siboni, A finite-strain constitutive theory for electro-active polymer composites via homogenization, Int. J. Non-Linear Mech. 47 (2) (2012) 293–306.
[39] C. Cao, X. Zhao, Tunable stiffness of electrorheological elastomers by designing mesostructures, Appl. Phys. Lett. 103 (4) (2013) 041901.
[40] O. Lopez-Pamies, Elastic dielectric composites: Theory and application to particle-filled ideal dielectrics, J. Mech. Phys. Solids 64 (2014) 61–82.
[41] B.-X. Xu, R. Mueller, M. Klassen, D. Gross, On electromechanical stability analysis of dielectric elastomer actuators, Appl. Phys. Lett. 97 (16) (2010) 162908.
[42] B.-X. Xu, R. Mueller, A. Theis, M. Klassen, D. Gross, Dynamic analysis of dielectric elastomer actuators, Appl. Phys. Lett. 100 (11) (2012) 112903.
[43] J.-S. Plante, S. Dubowsky, Large-scale failure modes of dielectric elastomer actuators, Int. J. Solids Struct. 43 (25–26) (2006) 7727–7751.
[44] K. Bertoldi, M. Gei, Instabilities in multilayered soft dielectrics, J. Mech. Phys. Solids 59 (1) (2011) 18–42.
[45] W. Li, C.M. Landis, Deformation and instabilities in dielectric elastomer composites, Smart Mater. Struct. 21 (9) (2012) 094006.
[46] S. Rudykh, K. Bhattacharya, G. deBotton, Multiscale instabilities in soft heterogeneous dielectric elastomers, Proc. R. Soc. Lond., Ser. A Math. Phys. Eng. Sci. 470 (2162) (2014) 20130618.
[47] R.J.M. Smit, W.A.M. Brekelmans, H.E.H. Meijer, Prediction of the mechanical behavior of nonlinear heterogeneous systems by multi-level finite element modeling, Comput. Methods Appl. Mech. Engrg. 155 (1998) 181–192.
[48] C. Miehe, J. Schotte, J. Schröder, Computational micro-macro transitions and overall moduli in the analysis of polycrystals at large strains, Comput. Mater. Sci. 16 (1–4) (1999) 372–382.
[49] C. Miehe, J. Schröder, J. Schotte, Computational homogenization analysis in finite plasticity. Simulation of texture development in polycrystalline materials, Comput. Methods Appl. Mech. Engrg. 171 (1999) 387–418.
[50] J.C. Michel, H. Moulinec, P. Suquet, Effective properties of composite materials with periodic microstructure: a computational approach, Comput. Methods Appl. Mech. Engrg. 172 (1999) 109–143.
[51] J. Schröder, Homogenisierungsmethoden der nichtlinearen Kontinuumsmechanik unter Beachtung von Instabilitäten. Habilitation, Bericht aus der Forschungsreihe des Instituts für Mechanik (Bauwesen), Lehrstuhl I, Universität Stuttgart, 2000.
[52] K. Terada, N. Kikuchi, A class of general algorithms for multi-scale analyses of heterogeneous media, Comput. Methods Appl. Mech. Engrg. 190 (40–41) (2001) 5427–5464.
[53] C. Miehe, A. Koch, Computational micro-to-macro transitions of discretized microstructures undergoing small strains, Arch. Appl. Mech. 72 (4) (2002) 300–317.
[54] V. Kouznetsova, M.G.D. Geers, W.A.M. Brekelmans, Multi-scale constitutive modelling of heterogeneous materials with a gradient-enhanced computational homogenization scheme, Int. J. Numer. Methods Eng. 54 (8) (2002) 1235–1260.
[55] K. Terada, I. Saiki, K. Matsui, Y. Yamakawa, Two-scale kinematics and linearization for simultaneous two-scale analysis of periodic heterogeneous solids at finite strain, Comput. Methods Appl. Mech. Engrg. 192 (31–32) (2003) 3531–3563.
[56] D. Markovic, R. Niekamp, A. Ibrahimbegovic, H.G. Matthies, R.L. Taylor, Multi-scale modeling of heterogeneous structures with inelastic constitutive behavior, Int. J. Comput.-Aided Eng. Softw. 22 (5/6) (2005) 664–683.
[57] D.D. Somer, E.A. de Souza Neto, W.G. Dettmer, D. Peric, A sub-stepping scheme for multi-scale analysis of solids, Comput. Methods Appl. Mech. Engrg. 198 (9–12) (2009) 1006–1016.
[58] J. Schröder, A numerical two-scale homogenization scheme: the FE^2-method, in: J. Schröder, K. Hackl (Eds.), Plasticity and Beyond, in: CISM International Centre for Mechanical Sciences, vol. 550, Springer Vienna, 2014, pp. 1–64.
[59] I. Özdemir, W.A.M. Brekelmans, M.G.D. Geers, Computational homogenization for heat conduction in heterogeneous solids, Int. J. Numer. Methods Eng. 73 (2) (2008) 185–204.
[60] I. Özdemir, W.A.M. Brekelmans, M.G.D. Geers, FE^2 computational homogenization for the thermo-mechanical analysis of heterogeneous solids, Comput. Methods Appl. Mech. Engrg. 198 (34) (2008) 602–613.
[61] J. Schröder, Derivation of the localization and homogenization conditions for electro-mechanically coupled problems, Comput. Mater. Sci. 46 (3) (2009) 595–599.
[62] J. Schröder, M.-A. Keip, Two-scale homogenization of electromechanically coupled boundary value problems, Comput. Mech. 50 (2012) 229–244.
[63] A. Javili, G. Chatzigeorgiou, P. Steinmann, Computational homogenization in magneto-mechanics, Int. J. Solids Struct. 50 (25–26) (2013) 4197–4216.
[64] Y.H. Pao, in: S. Nemat-Nasser (Ed.), Electromagnetic Forces in Deformable Continua, in: Mechanics Today, vol. 4, Pergamon Press, Oxford, 1978, pp. 209–306.
[65] M.-A. Keip, Modeling of electro-mechanically coupled materials on multiple scales, (Ph.D. thesis), Institute of Mechanics, Department Civil Engineering, University of Duisburg–Essen, 2012.
[66] R. Hill, Elastic properties of reinforced solids – some theoretical principles, J. Mech. Phys. Solids 11 (1963) 357–372.
[67] A. Ask, R. Denzer, A. Menzel, M. Ristinmaa, Inverse-motion-based form finding for quasi-incompressible finite electroelasticity, Int. J. Numer. Methods Eng. 94 (6) (2013) 554–572.